Tension thickening, molecular shape, and flow birefringence of an H-shaped polymer melt in steady shear and planar extension

Chunggi Baig and Vlasis G. Mavrantzas

Articles you may be interested in

Nonequilibrium molecular dynamics simulation of dendrimers and hyperbranched polymer melts undergoing planar elongational flow
J. Rheol. **58**, 281 (2014); 10.1122/1.4860355

Cross-slot extensional rheometry and the steady-state extensional response of long chain branched polymer melts
J. Rheol. **55**, 875 (2011); 10.1122/1.3589972

Coarse-grained molecular dynamics simulations of polymer melts in transient and steady shear flow
J. Chem. Phys. **118**, 10276 (2003); 10.1063/1.1572459

Uncrossability constraints in mesoscopic polymer melt simulations: Non-Rouse behavior of C 120 H 242
J. Chem. Phys. **115**, 2846 (2001); 10.1063/1.1385162

Steady-state behavior of dilute polymers in elongational flow. Dependence of the critical elongational rate on chain length, hydrodynamic interaction, and excluded volume
J. Rheol. **43**, 339 (1999); 10.1122/1.550987

Tension thickening, molecular shape, and flow birefringence of an H-shaped polymer melt in steady shear and planar extension

Chunggi Baig[a),b)] and Vlasis G. Mavrantzas[a),c)]
*Department of Chemical Engineering, University of Patras and FORTH-ICE/HT,
Patras, GR 26504, Greece*

Despite recent advances in the design of extensional rheometers optimized for strain and stress controlled operation in steady, dynamic, and transient modes, obtaining reliable steady-state elongational data for macromolecular systems is still a formidable task, limiting today's approach to trial-and-error efforts rather than based on a deep understanding of the deformation processes occurring under elongation. Guided, in particular, by the need to understand the special rheology of branched polymers, we studied a model, unentangled H-shaped polyethylene melt using nonequilibrium molecular dynamics simulations based on a recently developed rigorous statistical mechanics algorithm. The melt has been simulated under steady shear and steady planar extension, over a wide range of deformation rates. In shear, the steady-state shear viscosity is observed to decrease monotonically as the shear rate increases; furthermore, the degree of shear thinning of the viscosity and of the first- and second-normal stress coefficients is observed to be similar to that of a linear analog of the same total chain length. By contrast, in planar extension, the primary steady-state elongational viscosity η_1 is observed to exhibit a tension-thickening behavior as the elongation rate $\dot{\varepsilon}$ increases, which we analyze here in terms of (a) perturbations in the instantaneous intrinsic chain shape and (b) differences in the stress distribution along chain contour. The maximum in the plot of η_1 with $\dot{\varepsilon}$ occurs when the arm-stretching mode becomes active and is followed by a rather abrupt tension-thinning behavior. In contrast, the second elongational viscosity η_2 shows only a tension-thinning behavior. As an interesting point, the simulations predict the same value for the stress optical coefficient in the two flows, revealing an important rheo-optical characteristic. In agreement with experimental indications on significantly longer systems, our results confirm the importance of chain branching on the unique rheological properties of polymer melts in extension. © *2010 American Institute of Physics*. [doi:10.1063/1.3271831]

I. INTRODUCTION

Reliable and accurate data for the extensional rheology of polymer solutions and melts (e.g., adhesives, surfactants, hydrogels, bifunctional fluid-fluid interfaces based on short designed peptides, etc.) are of tremendous importance in the scientific design of new higher-value materials,[1,2] as most practical processing operations involve significant extensional deformations. Compared to their response in shear, polymer molecules under elongation exhibit many unusual properties such as strain hardening[1] and flow-induced crystallization.[3–6] An extensional flow can also cause polymer scission,[7,8] significant protein unfolding,[9–11] replication of DNA molecules,[12,13] etc. Fundamental information about viscosity, elasticity, recoverable stress, birefringence, and fracture in multiaxial elongational flow fields is thus absolutely necessary for polymer industries in order to evaluate new products and decisively pursue their design. To this, in addition to knowing the dependence of extensional behavior on external parameters (like applied strain rate, time, and

temperature), one should also know how molecular-level parameters (e.g., chemical structure, molecular architecture, molecular weight, branching, and polydispersity) affect rheological response. Unfortunately, from an experimental point of view, measuring the (steady-state) extensional properties of polymers is an extremely difficult task due to a number of issues,[1,14,15] the most important of which being that extensional deformations are inherently unstable due to the formation of a neck in the sample undergoing elongation; furthermore, the material may not deform homogeneously. This significantly limits the range of operation of extensional rheometers and the maximum Hencky strain that can be probed, and much labor is required on the measurements to achieve experimental control; in most of the experiments and tests the material breaks before a ('true') steady-state is attained.

All these explain the intense efforts in the last 40 years to develop accurate elongational rheometers for better quality data over a wide range of stress and strain rates and to increase the maximum extensional strains for which the sample deforms homogenously.[16–21] We mention, for example, that it is possible today to obtain quite accurate elongational data up to a Hencky strain of $\varepsilon = 7$, corresponding to a ratio of final-to-initial sample length of $\sim 1100(!)$, for low-density polyethylene (LDPE) melts under uniaxial

elongation.[1,19] It is generally accepted, however, that reliable steady-state elongational data for polymer melts are still missing. Even in cases where steady-state elongational properties (especially for some branched polymers, e.g., LDPE) have been reported in the literature with advanced rheometers,[22] it is still debatable whether these are true steady-state extensional data or not.[1,15,19] From a theoretical point of view, recent studies[23,24] have shown that making use of reliable steady-state elongational properties is also essential in evaluating viscoelastic models or in developing new ones.

Nowadays, the necessity for reliable extensional data has become even more imperative. The growing interest in the unique and unusual rheological properties of branched polymers in extension (thanks to technical advances in polyolefin synthesis which allowed the design and production of polymers with highly controlled architectures such as H-shaped combs and stars) opened new issues concerning the relationship between rheological properties and molecular architecture (especially for the role of branching on the processing characteristics of the melt).[25] This is because, according to existing experimental data,[1,25,26] chain branching seems to play a particularly important role in extensional flows. Branched polymers offer the possibility for simultaneous stress hardening and shear softening, which renders them highly attractive for practical operations due to greater control on processing properties. In addition to the growing amount of experimental data, this justifies also the development of highly sophisticated theoretical frameworks and models aimed at explaining the remarkable viscoelastic properties of branched polymers based on molecular arguments. An example is the pom-pom model (and its improvements),[25] an extension of the tube model proposed by de Gennes[27] and Doi and Edwards[28] for entangled linear polymers to polymers possessing a high molecular weight backbone to which a number of side arms is attached (comblike or H-shaped polymers). This is achieved by systematically introducing into the reptation model two new characteristic time scales in addition to the (longest) backbone orientation (or reptation) time: one associated with backbone stretching and another associated with arm withdrawal or retraction. For times longer than the longest arm retraction time, the backbone is free to diffuse; this motion is controlled by the effective frictional drag of the branch points, which typically far outweighs segmental frictional drag from the backbone itself.[29]

The pom-pom model provides a satisfactory description of the linear and nonlinear rheology of highly entangled comblike and H-shaped polymers by recognizing the importance of two fundamental mechanisms for relaxation in these systems: reptation and arm fluctuation. As nicely described by McLeish and Milner,[30] being underpinned on the tube model, such a treatment underlines the role of the renormalization of the dynamics on the hierarchy of the pertinent or relevant time scales. To get more fundamental physical insight into the role of side branches on the extensional rheology of polymer melts, we present here results for the steady-state shear and elongational properties of an H-shaped polyethylene melt, from direct nonequilibrium molecular dynamics (NEMD) simulations with a powerful, fully parallelized multiple time step algorithm. H-shaped is the simplest model structure for a branched polymer chain, yet capable of revealing the essential role of branches on the dynamics of nonlinear polymer melts: the chain consists of a main backbone which connects two branch points (or junctions), from each one of which two dangling arms (or branches) emanate. The system that we simulated here is an H-shaped polyethylene melt whose chains contain 78 carbon atoms along their main backbone and 25 carbon atoms along each one of their four dangling arms; we denote it as H_78_25 PE. The chain length has been deliberately selected to lie in the unentangled regime in order to separate out reptation phenomena from the dynamics and thus place the emphasis on atomistic interactions and their interplay with local chain conformation and architecture.

II. SIMULATION DETAILS

The NEMD simulations have been based on a rigorous statistical mechanics algorithm, called p-SLLOD algorithm,[31] alongside with appropriate boundary conditions which are the Lees–Edwards sliding-brick boundary conditions[32] for the case of shear [or planar Couette flow (PCF)] and the Kraynik–Reinelt spatial-temporal periodic boundary conditions[33–35] for the case of planar extensional flow (PEF). The following set of the p-SLLOD equations of motion was employed in our *NVT* NEMD simulations at constant temperature and density,

$$\dot{\mathbf{q}}_{ia} = \frac{\mathbf{p}_{ia}}{m_{ia}} + \mathbf{q}_{ia} \cdot \nabla \mathbf{u},$$

$$\dot{\mathbf{p}}_{ia} = \mathbf{F}_{ia} - \mathbf{p}_{ia} \cdot \nabla \mathbf{u} - m_{ia} \mathbf{q}_{ia} \cdot \nabla \mathbf{u} \cdot \nabla \mathbf{u} - \frac{p_\zeta}{Q} \mathbf{p}_{ia},$$

$$\dot{\zeta} = \frac{p_\zeta}{Q}, \qquad\qquad\qquad\qquad\qquad\qquad (1)$$

$$\dot{p}_\zeta = \sum_i \sum_a \frac{\mathbf{p}_{ia}^2}{m_{ia}} - dNk_BT,$$

where $\mathbf{q}_{ia}$, $\mathbf{p}_{ia}$, and $\mathbf{F}_{ia}$ are the position, momentum, and force vectors of atom a in molecule i, respectively, of mass m_{ia}, and V is the system volume. d denotes the space dimensionality, N the total number of atoms, T the absolute temperature, and k_B the Boltzmann constant. ζ and p_ζ are the coordinate- and momentum-like variables, respectively, of the Nosé–Hoover thermostat which controls the temperature of the system at the desired value and is known as the only one that can generate the true canonical ensemble (i.e., at constant temperature T and density ρ), and $Q = dNk_BT\tau^2$ is the mass parameter of the thermostat (τ, the relaxation time parameter, was set equal to 0.24 ps in the simulations). $\nabla \mathbf{u}$ represents the velocity gradient tensor of the imposed flow field:

$$\nabla \mathbf{u} = \begin{bmatrix} 0 & 0 & 0 \\ \dot{\gamma} & 0 & 0 \\ 0 & 0 & 0 \end{bmatrix} \quad \text{for PCF,} \tag{2a}$$

$$\nabla \mathbf{u} = \begin{bmatrix} \dot{\varepsilon} & 0 & 0 \\ 0 & -\dot{\varepsilon} & 0 \\ 0 & 0 & 0 \end{bmatrix} \quad \text{for PEF.} \tag{2b}$$

Note that in the case of PCF, the term $m_{ia}\mathbf{q}_{ia} \cdot \nabla \mathbf{u} \cdot \nabla \mathbf{u}$ in the momentum equation, Eq. (1), vanishes.

From a rheological point of view, PEF is more informative since it provides data for the two viscosity functions (the first and the second planar elongational viscosities) as opposed to only one viscosity function in the case of uniaxial or biaxial elongational flows. The well-known TraPPE united-atom force field for branched alkanes[36] was employed in the simulations. Also, in all simulations, a large number of molecules in a rectangular simulation box enlarged in the flow (x-) direction were considered to avoid system-size effects, especially at high strain rates where chains become highly stretched and aligned. Based, in particular, on the length ($|\mathbf{R}|_{\max} = 164$ Å) of the fully extended chain [a chain in the all *trans*-conformation with the equilibrium values for the C–C bond length (1.54 Å) and the C–C–C bending angle (114°)] and on the mean chain end-to-end distance at equilibrium ($\langle R^2 \rangle_{eq}^{1/2} = 50 \pm 1$ Å at $T = 450$ K), we considered up to 162 chains in a simulation box with dimensions $197.7 \times 65.9 \times 65.9$ Å^3 ($x \times y \times z$) in the PCF simulations and up to 294 chains in a box with dimensions $153.7 \times 153.7 \times 65.9$ Å^3 in the PEF simulations. That is, the box dimension along the x (the stretching) direction was chosen to be practically equal to $|\mathbf{R}|_{\max}$ while that along the other two (neutral or contracting) dimensions about 30% larger than $\langle R^2 \rangle_{eq}^{1/2}$. The system was maintained at density $\rho = 0.7818$ g/cm^3 and temperature $T = 450$ K (i.e., approximately 30–40 °C above its equilibrium melting temperature based on available experimental data),[37,38] and was fully equilibrated before it was subjected to flow. The set of the evolution equations (including also the equation for the Nosé–Hoover thermostat) was numerically integrated using the reversible reference system propagator algorithm[39] with two different time scales for an MD step; the large and small time steps were set equal to 2.39 and 0.48 fs for PCF, and equal to 2.30 and 0.46 fs for PEF, respectively (for more details on the NEMD methodology, readers are referred to the original papers in Refs. 31 and 35). The response of the system was investigated over a broad range of strain rates corresponding to Weissenberg numbers (Wi) in the intervals $0.5 \leq \text{Wi} \leq 13800$ for the PCF simulations and $0.2 \leq \text{Wi} \leq 3000$ for the PEF simulations. Wi is defined as $\text{Wi} \equiv \lambda \dot{\varepsilon}$ ($\dot{\varepsilon}$, the elongation rate) for the PEF simulations and as $\text{Wi} \equiv \lambda \dot{\gamma}$ ($\dot{\gamma}$, the shear rate) for the PCF simulations, where $\lambda = 33 \pm 1.5$ ns as estimated by the integral below the stretched-exponential curve describing the autocorrelation function for the chain junction-to-junction vector. Special care was taken to carry out the MD run for sufficiently long times (e.g., up to 192 ns, corresponding to 80×10^6 of MD steps, for the lowest strain rates studied in PCF) in order to
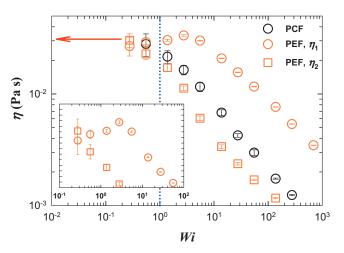

FIG. 1. Steady-state viscosity as a function of the dimensionless strain rates in the PCF and PEF. The red arrow indicates the prediction of the Rouse model. The steady-state tension thickening behavior of the dominant viscosity (η_1) in PEF is clearly observed (see the inset), while the second planar elongational viscosity (η_2) and the shear viscosity (η_{shear}) show only the tension and shear thinning behaviors, respectively. The blue vertical line indicates the characteristic point of Wi = 1 for which various nonlinear rheological behaviors usually start to show up.

reach state-state conditions and accumulate good statistics for the subsequent calculations of the properties of interest through ensemble averaging.

III. RESULTS AND DISCUSSION

Figure 1 presents results for the steady-state viscosity functions of the H_78_25 PE melt in the two flows. The shear viscosity, defined as $\eta_{\text{shear}} \equiv -\sigma_{xy}/\dot{\gamma}$, where $\boldsymbol{\sigma}$ denotes the stress tensor which is calculated by $\boldsymbol{\sigma} = \langle (1/V) \Sigma_i \Sigma_a ((\mathbf{p}_{ia}\mathbf{p}_{ia}/m_{ia}) + \mathbf{q}_{ia}\mathbf{F}_{ia}) \rangle$, is shown to monotonically decrease with increasing shear rate, indicative of the well-documented shear thinning behavior for practically all polymer melts (linear and branched).[1,14] We further report (results not shown here) that the degree of shear thinning for the viscosity and the first- and second-normal stress coefficients of the simulated melt (H_78_25) was similar to that of linear PE melts simulated in the recent past (for example, $C_{78}H_{158}$ and $C_{128}H_{258}$).[40] The branching effect on the shear rheology appears therefore to be relatively minor. This is in sharp contrast with the PEF results, where the branching effect is observed to be very important. As Fig. 1 shows, although the second planar elongational viscosity $\eta_2 \equiv (\sigma_{yy} - \sigma_{zz})/2\dot{\varepsilon}$ decreases monotonically with strain rate $\dot{\varepsilon}$ (indicative of a tension-thinning behavior, similarly to the shear viscosity), the first planar elongational viscosity $\eta_1 \equiv (\sigma_{xx} - \sigma_{yy})/4\dot{\varepsilon}$ initially increases with strain rate (indicative of a tension-thickening behavior), reaches a maximum at an intermediate value of the strain rate (Wi $\approx$ 3), and then starts to decrease by further increasing $\dot{\varepsilon}$ (indicative of a tension-thinning behavior). These results are supposed to resolve the long-time standing issue in the field whether or not the tension-thickening behavior exhibited by many branched polymers in elongational flows is true; it is clearly true! Even for the short, unentangled branched H_78_25 PE melt studied here, the NEMD data demonstrate that chain branching results in an increase of the dominant viscosity (η_1) with
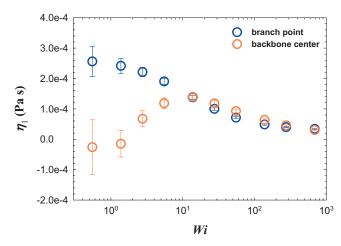
FIG. 2. Comparison between the contributions of branch point and interior backbone atoms (near the backbone middle point) to the first elongational viscosity η_1 in planar extension. The stress tensor contributed by the branch points was calculated by considering only up to seven atoms on each of the three chain segments around the junction points, i.e., 22 atoms in total per junction, and correspondingly the contribution by the main backbone was calculated by considering only seven atoms on each side of the backbone central atom, i.e., 15 atoms in total. The average-per-atom results (and after dividing with the applied strain rate to convert to viscosity units) are depicted in the plot.

extension rate, a phenomenon which, in fact, is also predicted by several existing macroscopic models[24,41,42] in a certain range of their parameter space. This is considered as an important finding (especially from the point of view of theoretical modeling), since it proves that it is not only mechanisms (such as arm withdrawal and backbone stretching) of relevance to entangled state that cause (both transient and steady-state) stress thickening: Given that the phenomenon shows up even in unentangled systems, we understand that it is more generic thereby calling for a clearer conception of the role of chain branching on polymer dynamics.

Another conclusion that we can draw from the simulation results displayed in Fig. 1 is that the degree of tension-thinning of the two elongational viscosities (η_1 and η_2) in the nonlinear regime is smaller than that of the shear viscosity (η_{shear}). Indeed, the exponent b in the power law expression $\eta \sim \dot{\gamma}^b$ or $\dot{\varepsilon}^b$ is calculated to be 0.50 for η_{shear}, 0.46 for η_1, and 0.43 for η_2 from the simulation curves while the corresponding zero-strain rate (or Newtonian) viscosities come out to be $\eta_{shear,0} \approx 0.028 \pm 0.007$ Pa s, $\eta_{1,0} \approx 0.027 \pm 0.005$ Pa s, and $\eta_{2,0} \approx 0.030 \pm 0.005$ Pa s, respectively. It is further seen that η_1 is larger than both η_2 and η_{shear} while η_2 is smaller than η_{shear}; interestingly, this seems to bear some analogy with experimental transient elongational data reported in the literature[15] for highly entangled, long-chain branched polymers (like LDPE).

In an effort to understand the origin of the tension-thickening behavior of the dominant viscosity in PEF, we separately analyzed the diagonal (tensile) components of the stress tensors contributed by atoms in the neighborhood of the branch point and further away in the interior of the main backbone. The average-per-atom contributions to the viscosity are shown in Fig. 2. The results indicate that (a) viscosity values associated with atoms in the two junction points are significantly higher than viscosity values associated with at-

oms deeply in the main backbone (no such distinction was observed in the PCF simulations; the two contributions were indistinguishable there within the statistical uncertainty), and (b) it is the contribution to viscosity from stresses by backbone atoms that changes nonmonotonically with extension rate; the latter is in support of the importance of backbone stretching on extensional rheology as emphasized also in the pom-pom model.

For a deeper understanding on the nature of viscosity, we analyzed separately the individual contributions of the different interaction modes to the viscosity. Figure 3 shows that for both the shear and elongational viscosities, the bond-stretching and inter- and intramolecular Lennard-Jones (LJ) interactions make positive contributions whereas the bond-bending and bond-torsional interactions make negative contributions. The key feature in the figure is that, despite their different characteristics, all contributions show a pattern very similar to that of the total viscosity in both flows, with increasing Wi. More specifically, while all modes exhibit a thinning behavior (their magnitude decreases as Wi is increased) in the case of η_{shear} and η_2, a tension-thickening behavior followed by the tension-thinning is observed in the case of η_1. It consequently appears that the total viscosity in the two flows does not arise from the mixed combination of different patterns contributed from the different interaction modes but from the simple combination of the same pattern from all of them (a similar result was reported in a previous study[43] referring to short linear PE melts under PEF).

In Fig. 4, we examine the hydrostatic pressure [calculated as one-third of the trace of the stress tensor $\boldsymbol{\sigma}$] developing in the simulated H-polymer melt as a function of strain rate. In PCF, this pressure is initially observed to decrease with increasing shear rate, then to reach a shallow minimum at an intermediate shear rate, and eventually to increase upon further increasing the shear rate. This phenomenon can be understood by taking two competing effects into account:[35,43] (a) chain stretching and alignment along the flow direction, which causes an increase in the attractive (negative values) intermolecular interactions and thus a decrease in the pressure, and (b) chain rotation[44] and intermolecular collisions, which result in an increase in the hydrostatic pressure. A strikingly different feature, however, appears in the case of PEF where the hydrostatic pressure is seen to decrease continuously with increasing the elongation rate without going through a minimum. This has its source to the dominant effect of chain stretching and alignment over intermolecular collisions in elongational flows. Thus, in PEF, chains are stretched and aligned along the flow direction much more than in PCF, since no chain rotation takes place in planar extension. As a result, favorable (i.e., attractive) side-side intermolecular interactions between different chains or different branches along the same chain are significantly increased, which eventually overshadows the effect of intermolecular collisions.

We now turn our attention to the analysis of structural and chain conformational properties in the two flows. To this, in Fig. 5 we plotted three root-mean squared chain dimensions (normalized with their equilibrium values): the first (R_{ee}) refers to the chain end-to-end vector, the second (R_{bb})
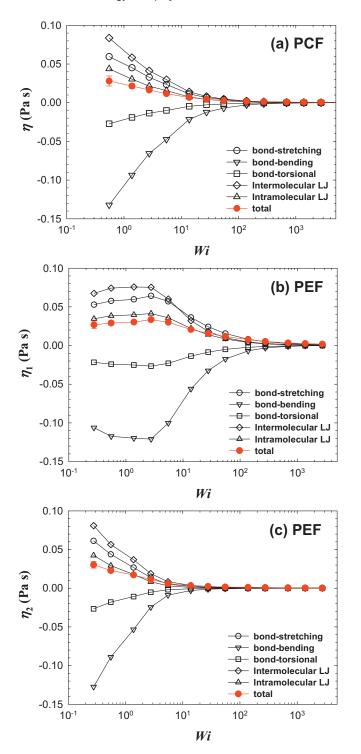
FIG. 3. Contribution of each interaction mode to the total viscosity: (a) to shear viscosity in PCF, (b) η_1 in PEF, and (c) η_2 in PEF.

FIG. 4. Plot of the hydrostatic pressure vs strain rate.

tional drag experienced by each junction point as they *diffuse* in the liquid (since they are accommodating the two dangling branches); this tends to increase the normalized junction-to-junction distance, and (b) the higher effective drag associated with the *rotational* motion of an H-chain due to branches (i.e., collisions with atoms of other chains); this causes the chain to stay longer in less favorable states (as far as its orientation is concerned), thereby resulting in a smaller value of the normalized end-to-end distance. In contrast, in the case of planar extension, the two quantities are equal only for low enough strain rates (smaller than about Wi ≈ 5). Beyond this, the average end-to-end distance becomes larger than the average junction-to-junction distance. This is explained as follows: for small enough strain rates, the short dangling arms can dissipate stresses (generated by the applied flow)

FIG. 5. Plots of the three root-mean-square distances (normalized with their equilibrium values) based on (a) the chain end-end-to-end distance (R_{ee}), (b) the chain branch-to-branch distance (R_{bb}), and (c) the overall chain radius of gyration (R_g). The results for PEF and PCF are represented by dark gray and black symbols, respectively. The error bars are smaller than the size of the symbols. Notice that, whereas the average R_{ee} and R_{bb} values are almost the same at all strain rates in PCF, they start to diverge at an intermediate strain rate in PEF. Remarkably, the value of the Wi number for which the average R_{ee} begins to increase faster than the average R_{bb} in PEF coincides with the point where the first extensional viscosity η_1 attains its maximum value (see Fig. 1), implying a phenomenological connection between the startup of the tension-thinning behavior in η_1 (macroscopic) and the arm-stretching mode (microscopic).

to the branch-to-branch vector, and the third (R_g) to the overall radius of gyration of the chain. In the case of shear, plots of the average R_{ee} and R_{bb} values as functions of the applied Wi number fall on top of each other in the whole range of strain rates. At first sight, this seems to contradict our intuition, according to which longer chain segments are stretched or deformed more than shorter chain segments at the same value of the applied strain rate. The apparent contradiction is resolved by considering (a) the higher stiffness of the junction-to-junction segment due to the higher effective fric-
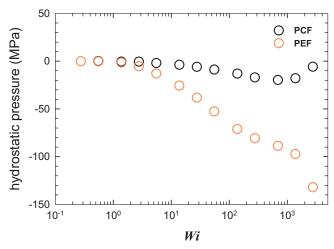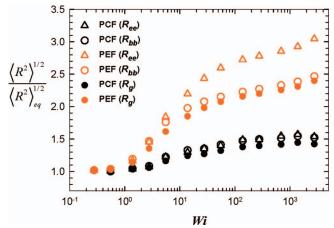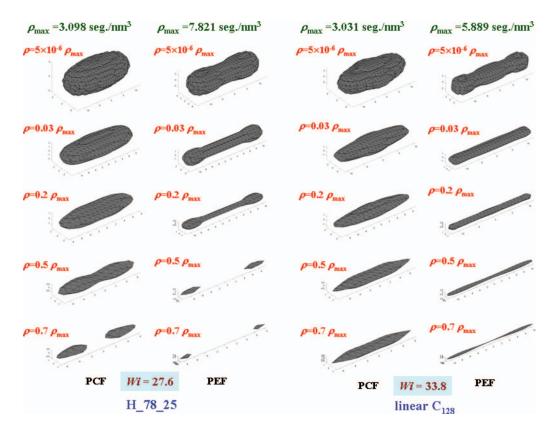
FIG. 6. Intrinsic molecular shapes of the H_78_25 PE melt under PCF and PEF at Wi=27.6, and of a C_{128} linear PE melt under PCF and PEF at Wi =33.8, based on isosurface plots computed at equal values of the (number-averaged) monomer (or segment) density in the frame of the principal axes (corresponding to the three eigenvectors) of the instantaneous radius of gyration tensor. The maximum segmental density ρ_{max} is equal to 3.098 segments/nm^3 under PCF and 7.821 segments/nm^3 under PEF for the H_78_25 melt, and equal to 3.031 segments/nm^3 under PCF and 5.889 segments/nm^3 for the C_{128} linear analog. Due to its rotational nature, PCF distorts the overall chain shape of both melts much less than the (irrotational) PEF. Moreover, a dumbbell-like shape (i.e., two dense cores with an extended thin neck or stem) is observed for the H_78_25 melt under PEF which should be contrasted with the more uniform and longer needlelike shape of the C_{128} linear melt subjected to the same type of flow.

rather quickly due to their fast relaxation; thus they are not significantly stretched or oriented by the flow. In this case, the overall chain dimension (i.e., the longest chain end-to-end distance) is mostly determined by the degree of stretching of the junction-to-junction segment. For strain rates, however, higher than the inverse of the arm relaxation time, junction-to-junction stretching is accompanied by significant deformation also of the four arms, which enhances the rate of increase of the average overall chain end-to-end distance with $\dot{\varepsilon}$.

A particularly noticeable phenomenon in the plots of Figs. 1 and 5 is that the value of the Wi number for which the average end-to-end distance begins to increase faster than the average branch-to-branch distance in PEF coincides with the point where the first (the dominant) extensional viscosity η_1 attains its maximum value. This result indicates that the steady-state tension-thinning behavior following the maximum of the dominant viscosity with $\dot{\varepsilon}$ when H-polymers are subjected to an extensional flow tends to begin when $\dot{\varepsilon}$ is such that the backbone-stretching mode slows down and the arm-stretching mode becomes active.

Additional information about the H-shaped chain structure as a function of strain rate is obtained by analyzing the normalized radius of gyration plots as shown in Fig. 5. It turns out that, both in shear and planar extension, the average value of R_g is close to that of R_{bb} for all deformation rates,

since most of the chain inertia is concentrated on (and therefore governed by) the backbone material (the material between the two junctions, i.e., the "cross-bar"). This underlines the importance of the dynamics of the backbone on the extensional rheology of branched polymers and is also in-line with the general assumptions of the pom-pom model[29] (which is, however, strictly valid only for highly entangled comblike or H-shaped polymers).

To gain additional insight into the structural changes induced by PEF, we analyzed the intrinsic molecular shape of the H_78_25 polymer. To this, we computed the segment cloud (the density distribution of segments around the chain center-of-mass) in the space of eigenvectors of the instantaneous radius of gyration tensor.[45,46] Results from this analysis are shown in Fig. 6 where three different sets of molecular shapes are displayed, verifying also what is known for random walks[47] that the intrinsic shape of the chains at equilibrium in the eigenvector space is far more like a "cake of soap" than like a spherical or ellipsoidal one of approximately Gaussian form. The first and second columns refer to the H_78_25 PE melt subjected to PCF and PEF, respectively, for a value of the Wi number equal to 27.6, while the third and fourth ones refer to a linear C_{128} PE melt subjected to PCF and PEF at a similar value of the Wi number (Wi=33.8). The C_{128} melt is considered here as the linear analog of the H_78_25 melt, since the same number (128) of

carbon atoms are included in the longest linear dimension of the chain in both melts. In all cases, the distributions are visualized as three-dimensional surfaces of constant segment density.[45,46] Clearly, in all cases, the applied flow field is strong enough to significantly perturb the intrinsic shape of the chains. It is also clear, however, that PEF exerts a stronger effect on the shape of the H_78_25 melt than PCF: Isosurfaces drawn at the same value of the segment density for this polymer are more perturbed (less ellipsoidal, more elongated) under PEF than under PCF. In fact, under PEF, the H_78_25 segment cloud (for low-to-intermediate values of the cloud density) assumes a characteristic arrangement wherein the two dense cores of highest density are connected with an extended stem. For even higher segment densities, this stem becomes thinner and thinner and eventually breaks. Under PCF, on the other hand, the isosurfaces have a different shape. At small segment density values, the density distribution is seen to be flattened along the longest principal axes (similar to that under equilibrium conditions). As the molecular shape is examined at higher values of the segment density, the distribution separates into two distinct regions, without clearly developing the thin stem or neck seen under PEF. For even higher values of the segment density, the two regions separate completely. Regarding the linear analog (the C_{128} melt) subjected to shear and planar extension, we notice that despite the little higher value of the Wi number for which isosurfaces in Fig. 6 are drawn for this system (Wi =33.8 as compared to Wi=27.6 for the H_78_25 melt), the characteristic arrangement of the two cores that are connected with an extended thin stem or neck observed in the case of the H_78_25 melt under PEF is lost. Instead, and compared to H_78_25 melt, the distribution in the linear melt under PEF is more uniform along the chain giving rise to an extended, needle-like shape which does not seem to break even when the cloud is examined at the highest segment densities. We believe that it is the gradual development of the two dense cores near the branch points and their higher drag coefficients that, together with the significant stretching of the backbone crossbar (the segment concentration along the backbone is clearly smaller than near the branch-points), results in the higher increase in the tensile stress along the backbone as the strain rate is increased. This leads eventually to the tension-thickening behavior exhibited by the H-polymer and to (primary) extensional viscosity values that are significantly higher compared to the shear viscosity ones (see Figs. 1 and 2).

Let us look next at how the flow field alters the potential energy of the system. Figure 7(a) compares the variation of the total potential energy as a function of strain rate in the two types of flow. We find that for the same value of the Wi number, the total energy change is larger in planar extension than in shear. Furthermore, while a slight minimum (followed by a maximum) shows up in the case of PCF (see inset), in the case of PEF a monotonic decrease is observed for all strain rates. In order to understand these peculiar phenomena, we separately investigated the different contributions to the potential energy. We consider first the nonbonded LJ energy. As shown in Fig. 7(b), the overall shape of the *intermolecular* part of the LJ energy under PCF and PEF can

be readily understood by taking into account the two competing effects (chain stretching or alignment and intermolecular collisions, as mentioned earlier for the hydrostatic pressure). We see that the higher degree of chain stretching and alignment in PEF produces larger (attractive) potential energy values due to enhanced side-side interactions, leading to a lower intermolecular LJ energy in this flow than in PCF. The correspondence to the hydrostatic pressure plots in Fig. 4 and the intermolecular LJ energy plots in Fig. 7(b) is in fact striking. [The correspondence is even more striking between hydrostatic pressure and bond-torsional energy plots, as shown below in Fig. 7(f)].

A more complicated trend is exhibited by the *intramolecular* LJ energy [Fig. 7(c)]. In both flows, this increases initially as the shear rate is increased, which is attributed to the larger chain deformations and the concomitant decrease in favorable (negative) interactions between atoms along the same chain. By further increasing the shear rate, a maximum is attained, beyond which the intramolecular LJ energy starts to decrease. This is due to the increase in the interaction energy between atoms belonging to different branches in the same chain as a result of their alignment parallel to the flow direction (in PCF this is further enhanced given the more compact chain structure due to chain rotation). By further increasing the Wi number causes the intramolecular LJ energy to pass through a minimum. Since chains at these high Wi values reach practically their fully oriented shape, the minimum is due to the (positive) energy contributions coming from intramolecular collisions between branch atoms. The minimum is more pronounced in PEF due to the higher degree of chain stretching and alignment achieved in this flow. Also, notice that in PEF both the maximum and the minimum occur at smaller strain rates than in PCF, indicative of the "stronger" type of planar extensional flow compared to shear flow. This can be seen also in Figs. 7(d)–7(f) showing how the three bonded components of the potential energy change with Wi. The overall shape of the bond-torsional energy, in particular, is very similar to that of the hydrostatic pressure shown in Fig. 4 both in PCF and PEF, implying that the hydrostatic pressure is intimately correlated with the global molecular shape. Another noticeable thing is the very small values attained by all types of the bonded interaction energies at the highest strain rates studied under PEF. This reflects smaller fluctuations in the bond lengths and bond angles around their equilibrium values together with the predominant all-*trans* (i.e., zig-zag) conformation of the chains in this flow. This might indicate the possibility for the development of flow-induced polymer crystallization in the system, something which has been observed recently in simulations with a short-chain ($C_{20}H_{44}$) linear PE melt at high enough strain rates,[5] although (to the best of our knowledge) no experimental report for such a phenomenon has appeared in the literature for H-polymers.

Lastly, in Fig. 8 we report results for the flow birefringence in the two flows for the simulated H_78_25 PE melt. To this, we plot the anisotropy $\Delta n = n_{xx} - n_{yy}$ in the refractive index tensor **n** as a function of the anisotropy $\Delta\sigma = \sigma_{xx} - \sigma_{yy}$ in the stress tensor $\boldsymbol{\sigma}$, and then compare the results for the
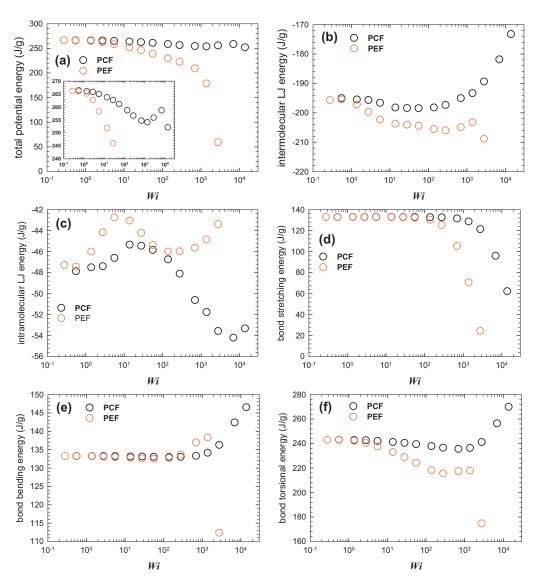
FIG. 7. Variation of the various interaction modes with strain rate in shear and planar extension: (a) total potential energy, (b) intermolecular LJ energy, (c) intramolecular LJ energy, (d) bond-stretching energy, (e) bond-bending energy, and (f) bond-torsional energy.

two flows. The figure shows that, to an excellent approxima-
tion, for small enough stresses (less than about 10 MPa), Δn
varies linearly with $\Delta \sigma$, a result which is known as the *stress
optical rule*. By fitting then the simulation data with straight
lines, we can obtain the stress optical coefficient C. The re-
sult is $C = (1.3 \pm 0.1) \times 10^{-9}$ Pa^{-1}, which turns out to be very
close to the value of $(1.37 \pm 0.10) \times 10^{-9}$ Pa^{-1} reported in
Ref. 48 for a $C_{50}H_{102}$ linear PE melt in shear. What is more
interesting, however, is that the value of C is the same in the
two flows. This is indeed a noteworthy observation, since in
PEF the linearity in the differences $\sigma_{xx} - \sigma_{yy}$ and $n_{xx} - n_{yy}$ of
the xx and yy components of the stress and birefringence
tensors, respectively, is attributed to the Newtonian response
of the system (at small strain rates), whereas in PCF the
appearance of a nonzero normal stress difference is a mani-
festation of its non-Newtonian behavior (even in the linear
regime). In the future, it would be worth confirming this
finding experimentally and/or verifying it for other poly-
meric materials (and also for other types of flow); if the trend
holds more generally, it would be very beneficial from a
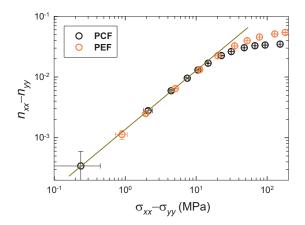practical point of view since we could execute more conve-

FIG. 8. Anisotropy in the refractive index (or birefringence) tensor **n** vs
anisotropy in the stress tensor $\boldsymbol{\sigma}$, in the simulated H_78_25 PE melt at T
=450 K in PCF and PEF, respectively. The birefringence tensor has been
calculated from the polarizability tensor determined by the average orienta-
tion of the (united) atomic C–C bonds via a rigorous mathematical formula
connecting the birefringence tensor with the polarizability tensor in aniso-
tropic materials (the overall procedure including the derivation of the for-
mula is described in detail in Ref. 48). The slope in the plot indicates the
linear relationship between **n** and $\boldsymbol{\sigma}$ (the stress-optical rule) at small stresses.

nient experiments and use the obtained information to predict the corresponding physical quantities under other complex flows.

IV. CONCLUSIONS

We presented a detailed NEMD simulation study which provides atomistic-level evidence for the steady-state tension-thickening behavior of H-shaped polymers under elongation. The most important result of the work is that the tension-thickening behavior shows up even for unentangled branched polymers. The maximum in the dominant elongational viscosity (η_1) is obtained for that value of the Wi number for which arm stretching begins. By analyzing the intrinsic shape of the simulated H-shaped melt in the frame of the eigenvectors of the principal axis of its radius of gyration tensor, we have been able to trace the deformation of its segment cloud distribution. We found that in contrast with their response to an applied shear flow, an H-shaped polymer melt subjected to planar extension exhibits significant perturbations of its intrinsic shape from the equilibrium one at the same value of the segment cloud density. Even at moderate values of the applied strain rate, a characteristic arrangement is observed in which two dense cores (loci of highest density) are connected by an extended thin stem or neck. This is observed for segment densities that are not too high (from the very small encompassing 2%–3% of the total segments, up to the intermediate still encompassing only 15%–20% of the total segments). In contrast, under an applied shear flow, this characteristic neck or stem (the dumbbell-shaped distribution) disappears and a hole appears between the two loci of highest density.

The above simulation findings support the generally accepted opinion today (mostly on the basis of transient experimental data) that branches make a stronger effect in an elongational flow than in shear. On the other hand, our results seem to call for a deeper understanding of the role of branches on the molecular rheology of branched polymers. For example, the fundamental molecular mechanisms addressed by the pom-pom model for H-polymers are chain reptation and branch retraction along the effective tube, phenomena which are practically effective only for deeply entangled polymers (i.e., polymers with very long branches and backbones). The present study which reveals a tension thickening behavior even in an unentangled H-shaped polymer (it contains only 25 carbon atoms along each branch) subject to an elongational flow seems to indicate the existence of additional mechanisms that one should consider in order to quantitatively capture the complicated rheology of branched polymers. For longer H-shaped polymer melts, it seems that the effects of reptation (which will be the dominant relaxation mechanism at long times for entangled molecules) will add up to the phenomena observed here and render them even more pronounced. For example, we expect the tension-thickening of the primary planar elongational viscosity η_1 shown in Fig. 1 and also the maximum in the contribution to η_1 from backbone atoms seen in Fig. 2 to be more striking. On the other hand, considering that a chain molecule (whether short or long) is likely to diffuse easier in the di-

rection of stretching and orientation (in the anisotropic environment induced by the flow field), our feeling is that all other interesting phenomena recorded in the present simulations with the unentangled H_78_25 melt are likely to be expected also in entangled H-polymers.

Of particular value is the NEMD simulation prediction that the value of the Wi number beyond which the magnitude of the normalized junction-to-junction distance deviates from that of the normalized end-to-end distance coincides with that for which the maximum in η_1 is observed. This implies that the tension-thinning behavior begins when the applied elongation rate is high enough to cause arm stretching. This is a significant prediction of the present study which, clearly, will be worth verifying in the future experimentally.

We further observed that the contribution to the total viscosity by the individual interaction modes follows a behavior which is similar to that of the viscosity itself, independent of the type of flow (shear or elongational). The prediction that the stress optical coefficient C based on the xx and yy components of the stress and birefringence tensors is equal in PCF and PEF is also another important result of our study.

[1] R. B. Bird, R. C. Armstrong, and O. Hassager, *Dynamics of Polymeric Liquids, Fluid Mechanics*, 2nd ed. (Wiley-Interscience, New York, 1987), Vol. 1.
[2] R. G. Larson, *The Structure and Rheology of Complex Fluids* (Oxford University Press, New York, 1999).
[3] F. L. Binsbergen, Nature (London) **211**, 516 (1966).
[4] B. S. Hsiao, L. Yang, R. H. Somani, C. A. Avila-Orta, and L. Zhu, Phys. Rev. Lett. **94**, 117802 (2005).
[5] T. C. Ionescu, C. Baig, B. J. Edwards, D. J. Keffer, and A. Habenschuss, Phys. Rev. Lett. **96**, 037802 (2006).
[6] S. Kimata, T. Sakurai, Y. Nozue, T. Kasahara, N. Yamaguchi, T. Karino, M. Shibayama, and J. A. Kornfield, Science **316**, 1014 (2007).
[7] A. Keller and J. A. Odell, Nature (London) **312**, 98 (1984).
[8] S. A. Vanapalli, S. L. Ceccio, and M. J. Solomon, Proc. Natl. Acad. Sci. U.S.A. **103**, 16660 (2006).
[9] L. Tskhovrebova, J. Trinick, J. A. Sleep, and R. M. Simmons, Nature (London) **387**, 308 (1997).
[10] M. Rief, M. Gautel, F. Oesterhelt, J. M. Fernandez, and H. E. Gaub, Science **276**, 1109 (1997).
[11] D. K. Klimov and D. Thirumalai, Proc. Natl. Acad. Sci. U.S.A. **96**, 6166 (1999).
[12] B. Maier, D. Bensimon, and V. Croquette, Proc. Natl. Acad. Sci. U.S.A. **97**, 12002 (2000).
[13] A. Goel, M. D. Frank-Kamenetskii, T. Ellenberger, and D. Herschbach, Proc. Natl. Acad. Sci. U.S.A. **98**, 8485 (2001).
[14] J. Meissner and J. Meissner, Pure Appl. Chem. **42**, 551 (1975).
[15] H. M. Laun and H. Schuch, J. Rheol. **33**, 119 (1989).
[16] J. Meissner, Rheol. Acta **8**, 78 (1969).
[17] J. Meissner, Trans. Soc. Rheol. **16**, 405 (1972).
[18] H. Münstedt, J. Rheol. **23**, 421 (1979).
[19] J. Meissner, T. Raible, and S. E. Stephenson, J. Rheol. **25**, 1 (1981).
[20] A. Bach, H. K. Rasmussen, and O. Hassager, J. Rheol. **47**, 429 (2003).
[21] D. G. Hassell and M. R. Mackley, Rheol. Acta **47**, 435 (2008).
[22] H. M. Laun and H. Münstedt, Rheol. Acta **17**, 415 (1978).
[23] C. Baig, B. Jiang, B. J. Edwards, D. J. Keffer, and H. D. Cochran, J.

Rheol. **50**, 625 (2006).

[24] P. S. Stephanou, C. Baig, and V. G. Mavrantzas, J. Rheol. **53**, 309 (2009).

[25] T. C. B. McLeish, Adv. Phys. **51**, 1379 (2002).

[26] H. Münstedt and H. M. Laun, Rheol. Acta **20**, 211 (1981).

[27] P. G. de Gennes, J. Chem. Phys. **55**, 572 (1971).

[28] M. Doi and S. F. Edwards, *The Theory of Polymer Dynamics* (Oxford University Press, New York, 1986).

[29] T. C. B. McLeish and R. G. Larson, J. Rheol. **42**, 81 (1998).

[30] T. C. B. McLeish and S. T. Milner, Adv. Polym. Sci. **143**, 195 (1999).

[31] C. Baig, B. J. Edwards, D. J. Keffer, and H. D. Cochran, J. Chem. Phys. **122**, 114103 (2005).

[32] A. W. Lees and S. F. Edwards, J. Phys. C **5**, 1921 (1972).

[33] A. M. Kraynik and D. A. Reinelt, Int. J. Multiphase Flow **18**, 1045 (1992).

[34] B. D. Todd and P. J. Daivis, Phys. Rev. Lett. **81**, 1118 (1998).

[35] C. Baig, B. J. Edwards, D. J. Keffer, and H. D. Cochran, J. Chem. Phys. **122**, 184906 (2005).

[36] M. G. Martin and J. I. Siepmann, J. Phys. Chem. B **103**, 4508 (1999).

[37] J. Pak and B. Wunderlich, Macromolecules **34**, 4492 (2001).

[38] G. T. Dee, T. Ougizawa, and D. J. Walsh, Polymer **33**, 3462 (1992).

[39] M. Tuckerman, B. J. Berne, and G. J. Martyna, J. Chem. Phys. **97**, 1990 (1992).

[40] J. M. Kim, D. J. Keffer, M. Kröger, and B. J. Edwards, J. Non-Newtonian Fluid Mech. **152**, 168 (2008).

[41] A. Souvaliotis and A. N. Beris, J. Rheol. **36**, 241 (1992).

[42] J. M. Wiest, Rheol. Acta **28**, 4 (1989).

[43] C. Baig, B. J. Edwards, D. J. Keffer, H. D. Cochran, and V. A. Harmandaris, J. Chem. Phys. **124**, 084902 (2006).

[44] J. M. Kim, B. J. Edwards, D. J. Keffer, and B. Khomami, Phys. Lett. A **373**, 769 (2009).

[45] D. N. Theodorou and U. W. Suter, Macromolecules **18**, 1206 (1985).

[46] V. G. Mavrantzas and D. N. Theodorou, Macromolecules **31**, 6310 (1998).

[47] K. Šolc and W. H. Stockmayer, J. Chem. Phys. **54**, 2756 (1971).

[48] C. Baig, B. J. Edwards, and D. J. Keffer, Rheol. Acta **46**, 1171 (2007).